A real-time ultrasound rendering with model-based tissue deformation for needle insertion

Charles Barnouin, Florence Zara, Fabrice Jaillet

A real-time ultrasound rendering with model-based tissue deformation for needle insertion

Charles Barnouin[1], Florence Zara[1][a] and Fabrice Jaillet[2][b]
[1]*Université de Lyon, CNRS, Université Lyon 1, LIRIS, SAARA team, UMR5205, F-69622, France.*
[2]*Université de Lyon, IUT Lyon 1, Computer Science Department, F-01000, Bourg-en-Bresse, France.*
{*f_author, s_author, t_author*}*@liris.cnrs.fr*

Keywords: Ultrasound rendering, 2D texture, haptic devices, physically based tissue deformation, needle insertion.

Abstract: In the course of developing a training simulator for puncture, a novel approach is proposed to render in real-time the ultrasound (US) image of any 3D model. It is combined with the deformation of the soft tissues (due to their interactions with a needle and a probe) according to their physical properties. Our solution reproduces the usual US artifacts at a low cost. It combines the use of textures and ray-tracing with a new way to efficiently render fibrous tissues. Deformations are handled in real-time on the GPU using displacement functions. Our approach goes beyond the usual bottleneck of real-time deformations of 3D models in interactive US simulation. The display of tissues deformation and the possibilities to tune the 3D morphotypes, tissue properties, needle shape, or even specific probe characteristics, is clearly an advantage in such a training environment.

1 Introduction

Ultrasound (US) is a radiation-free, non-invasive and real-time imaging medical device. Widely used in clinical practice, it is a mechanical wave propagating in fluids and solids generally at 20 kHz. Multiple tissue interactions create the final image, such as specular reflection and refraction, absorption and scattering. Relatively cost-effective, it is relevantly used for both diagnosis and image-guided interventions (Heer et al., 2004). Nevertheless, extensive training is required to acquire and interpret ultrasound images, especially when paired with the insertion of a needle. For example, the puncture necessitates spatial reasoning, hand-eye and left/right hand coordination, all skills developed through extensive training.

In the rheumatology domain, a relevant training simulator for needle insertion has to enable students to learn how to puncture from multiple points of view, and to identify tissues which properties may differ from a patient to another, or when tissues are inflamed. Moreover, the training environment has to provide interactive and accurate forces feedback through haptic devices: during puncture, the rheumatologists adapt their gesture to the deformations induced by the probe and needle movements. Thus, two challenges emerge to develop such a simulator: (i) render a realistic enough ultrasound image in any probe/tissues configuration, embedding all the properties to clearly identify the biological tissues; (ii) provide real-time interactions between the soft tissues and the medical devices through force feedback and visible deformations on the ultrasound image.

In this paper, we propose a new strategy to address these two points. We will describe our proposed solution for ultrasound rendering, haptic forces feedback and display of tissues deformation on the ultrasound images. All the components of our solution are linked and embodied in a coherent framework. At the end, our approach based on the GPU permits:

- a real-time ultrasound rendering including tissues fibrosity according to their geometrical properties. We used an original texture-dependent oriented blur to enhance realism.
- a visualization of tissues deformation directly on the ultrasound image. We used some displacement functions accounting for the tissues properties and the interaction forces between the haptic devices and the 3D scene.

Our solution has been designed to be easily transferable to multiple medical cases and areas of interest, such as the shoulder or ankle joints. It combines techniques from Computer Graphics rendering and Virtual Reality in a complementary way to provide realistic visual and touch sensations at the same time.

[a] https://orcid.org/0000-0002-0118-7204
[b] https://orcid.org/0000-0002-7330-8116

Ray-tracing and texture manipulation provide accurate enough tissue rendering for a real-time simulator, while the collision and haptic algorithms are suitable for a fast update necessary for a smooth touch feeling.

2 State of the art

This section presents previous work on ultrasound rendering and simulation of needle insertion. Both are combined to provide realistic tissue deformations and haptic feedback within an ultrasound view.

Ultrasound rendering. The techniques to create US image can be separated in two approaches: interpolation of real images or generation of realistic images.

The first approach uses pre-recorded 3D ultrasound volume, generally acquired with a 3D probe, or by combining multiple 2D slices. In some cases, the 3D volume can also be reconstructed from Computed Tomography (CT scan) or MRI acquisition. During the ultrasound rendering simulation, the volume is sliced along the plane created with the ultrasound probe. With this approach, in (Magee and Kessel, 2005), an augmented reality simulator matched a real CT scan with a mannequin body, whereas the probe was calibrated to find the location and orientation of the ultrasound plane to slice the volume. Later on, they improved the image quality with 3D textures obtained from real images (Magee et al., 2007). In (Ni et al., 2011), a biopsy simulator was embedding several ultrasound volumes scanned with a dedicated probe and stitched together to form a panorama. This panorama is then resampled to match a previously acquired CT scan of the same volume. Spacial transformations may be applied afterwards, to create respiratory motion for example. In (Vidal et al., 2008), an ultrasound guided needle puncture simulator with patient specific CT scan is proposed, which also requires an acquisition phase and remains very patient-dependent. They added several post-processing effects like shadows, but did not implement tissue deformation. In (Goksel and Salcudean, 2009), they used 3D ultrasound volumes matched to a 3D elasticity model to perform a fast B-Mode ultrasound image in deformable tissues. While being realistic for obvious reasons, this class of approach imposes constraints on the model, which needs to roughly match the database and to be created for every considered joint. Moreover, it requires to create a 3D volume for each new case, such as specific location of inflammatory tissues or patient specific geometry or morphology (aged or fat inflamed shoulders considerably differ from a healthy and young one). The specificity of the probe (field of view, frequency, area of effect, etc.) is also imposed by the acquisition probe.

The second approach to synthetic ultrasound images consists in simulating the ultrasonic wave propagation in the media, with accurate models of the probe, tissue scatterers, and interface models. Usually, generating a single frame is simply too time consuming for real-time applications. The older models may take up to several hours (Bamber and Dickinson, 1980; Jensen, 1991). However, new approaches are getting closer to real-time, such as (Marion and Vray, 2009), where a linear convolution model and a 3D set of moving scatterers were used, combined with better hardware. Others physical ray-tracing methods using GPU such as presented in (Mattausch and Goksel, 2016; Burger et al., 2013) are seen as very promising despite a loss of performance while dealing with tissue deformations. They used a combination of convolution and ray-tracing to create their render. Another interesting idea was presented in (Law et al., 2011) to render ultrasound images on deformable meshes, using two opposite rays for each pixel that needs to be rendered, one of them going towards the probe. They register the traversed materials to deduce the pixel color, and thus are able to create effects like attenuation. However, performances of this approach are not compatible with the requirements of a training simulator, especially when the probe is moving continuously. Finally, the ray-tracing methods don't take tissue fiber into account: as the number of surfaces goes higher, it would increase the number of bounces and thus the calculus time.

To go beyond the limitations of both approaches, such as the rigidity of 3D data volume for the former and computation time for the latter, we propose a novel approach combining the use of textures and ray-tracing to render ultrasound effects like shadows, speckle, and fiber orientation. Moreover, in the context of the development of a training medical simulator, real-time computation, as well as the possibility to tune the 3D models, the physical properties of tissues, or the probe characteristics (field of view, attenuation, etc.) are important points to consider.

Needle insertion simulation. Modeling techniques for puncture also face the accuracy *vs* real-time trade-off. Soft tissue cutting, due to the needle insertion, involves three types of force: frictional, elastic, and actual cutting forces. However, the cutting force is often modeled as a constant acting at the tip of the needle, and no actual tissue cutting is performed for performance reasons. In a review on cutting mechanics and techniques (Takabi and Tai, 2017), the *cohesive zone* model is seen as the most promising technique, though requiring to set up the cohesive zone before the cutting. Moreover, the step-by-step remeshing, used to prepare the zone, may be time-consuming,

and the simulation itself is not performed in real-time. Yet, needle insertion modeling for real-time application has been presented in (Abolhassani et al., 2007), which aims to address the modeling of the force as well as the needle path.

In one of the precursor works in puncture modeling (DiMaio and Salcudean, 2003), the force distribution is estimated along the shaft and a 2D model is proposed for force/displacement relationship. Later, Okamura *et al*. investigated the *in vitro* needle forces using sensors, and presented models for cutting, friction and elastic forces during puncture (Okamura et al., 2004). The strength of those models is that they are simple enough for real-time applications. A new method was presented in (Duriez et al., 2009) for the insertion of flexible needle using constraint models. They achieved a real-time simulation with deformable needle and tissue, while adding effect like steering. However, only a simple model was presented, and there is no evidence the method will keep working with more complex ones.

(Crouch et al., 2005), and later on (Gao et al., 2013) chose to study the tissue deformation in regard of time and insertion velocity. The former focuses on the insertion force once the needle is inside the tissue, while the latter insists on the deformation of the surface during puncture. Both studies are of particular interest: assuming the needle velocity being approximately constant during puncture, they can link tissue deformation and needle insertion with a simple mathematical function. Both authors assure a good approximation of force and deformation, even if the fidelity of the relaxation phase could be improved.

In our approach, the force feedback, due to the needle insertion in tissues, are calculated without changing the topology of the meshes involved in the 3D scene. Our solution is based on the use of displacement field models allowing us to handle deformation according to both physical properties (the force intensity) of the tissues and the organ shape (*via* the geometric mesh). It allows us a real-time display, and an accurate force model compatible with haptic requirements.

3 General approach

To propose a relevant training simulator of needle puncture, one of the challenges remains in generating an interactive 2D view of the 3D scene with a realist ultrasound rendering which must exhibit the tissues deformation involved by the manipulation of two haptic devices (simulating the probe and the needle).

At the beginning of each time frame, the first step consists in computing a 2D slice of the 3D scene according to the probe position. To that aim, a new surface is created for each 3D mesh of the scene using the *Capping Clipped Solids* method (McReynolds and Blythe, 2005, chapter 16). This *OpenGL* based solution enables a fast computation of the slices, and the new surfaces hence created will serve as support for the effects during the rendering pass, to integrate the tissues deformation and create the final ultrasound image. Moreover, the 2D slice is rendered in the same render pass as the 3D scene, which means both can be displayed concurrently without performance loss. This enables a nice two-views display inside the medical simulator. Next, Fig. 1 illustrates our pipeline strategy of creating, in real-time, a relevant ultrasound rendering with tissues deformation.

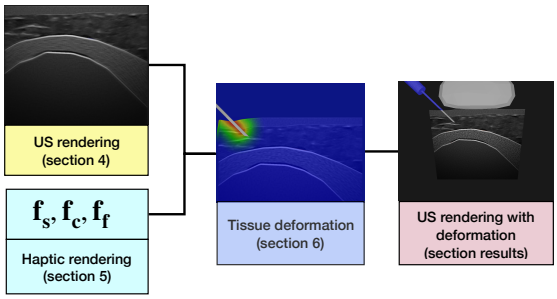

Figure 1: Our pipeline to obtain an ultrasound image of our 3D scene during the manipulation of the two haptic devices.

Ultrasound rendering (see section 4). The ultrasound view requires two steps. Firstly, we deal with a solution based on an ultrasound database limited to textures, to compute the ultrasound rendering on the 2D slice. Note that, no complete pre-recorded ultrasound volume is required. Secondly, some extra treatments are performed to consider the orientation of the tissues (with an original way to show fiber orientation for tendon using a texture-dependent oriented blur) or to add artifacts (like shadow or reflection) resulting from the manipulation of a probe. This approach enables the generation of the ultrasound view of any joints (shoulder, knee) in all directions according to the manipulation of the probe. Moreover, it only requires a few number of real ultrasound images.

Haptic rendering (see section 5). To reproduce the sense of touch and to improve the realism of the simulator, we provide haptic feedback of the probe and of the needle used during puncture. As these devices exhibit distinct behavior, the force-feedback algorithm would differ: the probe only experiences contact, while the needle goes through contact and insertion. Thus, frictional, elastic and cutting force are modeled for the needle, which is also path constrained with a *tunnel effect*. While the forces calculation is already well-known, the precision of

our collision algorithm and our *tunnel effect* allow us to easily transfer the force information to produce accurate visual deformations due to the interactions.

Tissue deformation (see section 6). The ultrasound view must display the deformations undergone by tissues due to the needle insertion during the puncture gesture, as well as probe/tissue interactions. To that end, we use the haptic devices feedback and we define two displacement functions that link the force to the displacement of the surrounding tissues. Then, the calculus of these deformations is performed on the GPU to create a specific output image. Finally, this 2D output image will be used to integrate these deformations into the ultrasound view. This approach, which is based on the deformation of the 2D image (rather than the simulation of 3D mesh deformations), enables us a real-time rendering of the tissues deformation.

Fig. 2 gives an illustration of the modules in our framework and the communications between them.

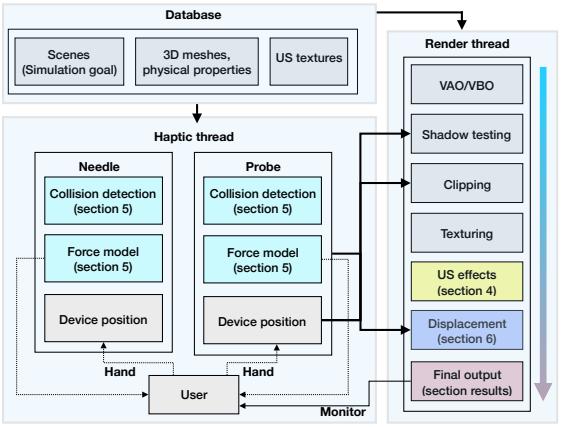

Figure 2: The modules of our framework.

4 Ultrasound rendering

In this section, we will detail our solution to create an US rendering of a 3D scene in real-time. It deals with ultrasound texture and additional treatments to further integrate usual ultrasound artifacts (Law et al., 2011).

Creation of our 3D scene. A simplified scene based on a young and healthy shoulder will serve to illustrate our rendering process. To create this scene, all tissues but subcutaneous fat were segmented from a reference US image. Then, the layers were extruded and turned into 3D meshes. At the end, it contains 4,004 tetrahedral elements for all the involved tissues (Fig. 3(3-8)). Next, our US rendering process runs in several steps, as illustrated on Fig. 4. It starts from the 2D slice of the 3D scene (Fig. 4a) on which several effects (reflection, shadow, attenuation, noise, blur, orientation) are added to obtain the US view (Fig. 4f).

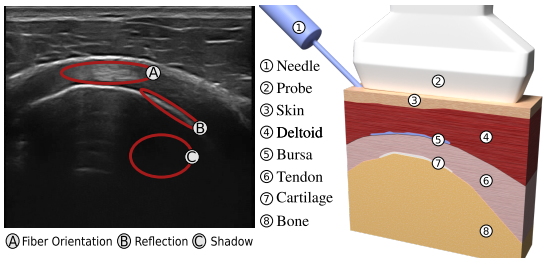

Ultrasound reference image

Figure 3: 3D view of the shoulder scene made from a US reference image. The probe and the needle have been added.

2D slice with diffuse color. The process starts from Fig. 4a with the 2D slice of our 3D scene (obtained according to the probe position). The 2D surfaces created by the *Capping Clipped Solids* method were given a diffuse color, except for the deltoid. Indeed, for thick tissue (like deltoid), we can directly apply a texture acquired from the reference image (Fig. 3(4)), by selecting a zone with a representative pattern for the tissue, and using a texture synthesis algorithm (Harrison, 2001). Thus, we use the similarity of the fibrous pattern in thick muscles for a given orientation to fill a texture data bank from reference images, and use those textures as a basis for the US images of any thick muscle. Two orientations were considered: lateral and longitudinal (respectively perpendicular and parallel to the US plane), due to differences in patterns. The diffuse color given to each of the other tissues is its target mean color in the final render, at the exception of the bone tissue, whose white color is the the reflection one.

Reflection and shadow. Reflection and refraction occur at the boundary of two media. In fluid/fluid interfaces, the reflection ratio increases with the difference of acoustic impedance between the media. Indeed, the intensity reflected I_r at the interface from an incoming intensity I_i is defined according to the acoustic impedance Z_1, Z_2 of each media with:

$$I_r = I_i \left(\frac{Z_2 - Z_1}{Z_2 + Z_1} \right)^2 . \quad (1)$$

Visually, a bright area appears at most of tissue interfaces (skin/muscle, muscle/tendon - Fig. 3(B)) due to this reflected intensity. For fluid/solid interfaces, when the ultrasound wave encounters a bone, most of the energy will be reflected. As a result, a darker area/shadow (Fig. 3(C)) appears below the bone surface, with a bright area on the bone interface itself.

To create both effects at the same time, a typical *depth map* is filled into a texture, before any other render pass (the US probe acting as a spotlight). This

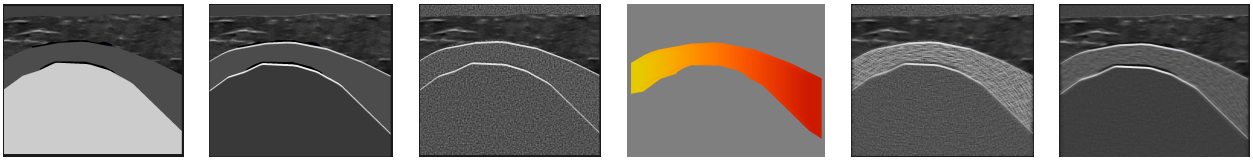

(a) 2D slice (b) = (a) + ref./sh. (c) = (b) + noise (d) fiber orientation (e) = (c) + (d) (f) = (b) + (e)

Figure 4: Illustration of the rendering pass effects to generate an US image. Contrast has been modified for a better view.

depth map contains information relative to the distance of the surfaces of objects to the probe. It provides feedback regarding which parts are lying underneath bones, for example. Later on, a ray-tracing is performed to trigger shadows in appropriate places. Let's note that a small bias was added to the depth testing to acknowledge the reflection phenomenon. While inside this bias, the render appears brighter.

This method allows us to create both the reflection and shadow rendering in one step for fluid/solid interfaces. For a fluid/fluid interface, only the bright area is rendered: *e.g.* tendons appear as hyperechoic (bright) but get no shadow. In our example, applying these effects on Fig. 4a leads to Fig. 4b.

Attenuation. When the US wave propagates through the tissues, the acoustic pressure undergoes an attenuation of its global amplitude. Attenuation gathers two ultrasound phenomena: scattering and absorption.

Scattering. The scattering effect results from the interaction of the wave with the small particles or defaults in the biological tissue. Their physical properties are different enough from the surrounding medium to lead to the emission of a secondary wave. It creates the speckle effect in the US images, which is computationally intensive to recreate accurately. In our rendering, the speckle is approximated by a Perlin noise: from Fig. 4b, we obtained Fig. 4c.

Absorption. This effect depends on the frequency f of the probe, the biological tissue characteristics and the distance to the wave emission point. With attenuation coefficient α and depth z , the attenuation intensity I_a from an incoming intensity I_i is defined by:

$$I_a = I_i \cdot 10^{-\alpha z f/20}. \quad (2)$$

Visually, it generates darker pixels as the wave propagates further. A non physically-realistic but cost effective and accurate enough visual effect can be achieved with the help of the same ray-tracing as in the *shadow rendering* pass. Indeed, knowing the distance between the pixel to be rendered and the probe, it is enough to use only the average soft tissue attenuation for each tissue in the scene. The attenuation effect is added at the end of the rendering process: with Fig. 5a (identical to Fig. 4f), we obtained Fig. 5b (using $\alpha = 0.54$ db/(MHz.cm)).

Fiber orientation. As previously explained for deltoid, longitudinal and lateral 2D textures are extracted and synthesized beforehand from real ultrasound recording to consider the orientation of some biological thick tissues like muscles. Then, the right texture blending ratio is computed relatively to the the tissue orientation θ with the probe (see Fig. 6). However, the texture synthesis failed for thin tissues (like tendons - Fig. 3(A-6)) since the input data are too scarce. A way to achieve the desired visual orientation would be to model all lines inside the fibrous model. However, this would force us to create numerous lines inside each fibrous tissue prior to the rendering pass, thus dramatically reducing performances. Instead, we proposed a new method that we called *oriented blur*.

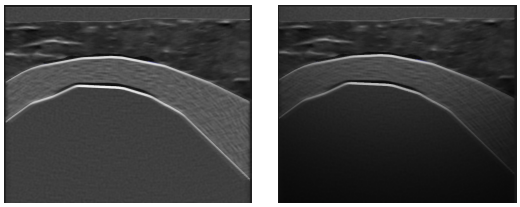

(a) w/o absorption (b) w/ absorption

Figure 5: US image without (a) or with (b) absorption.

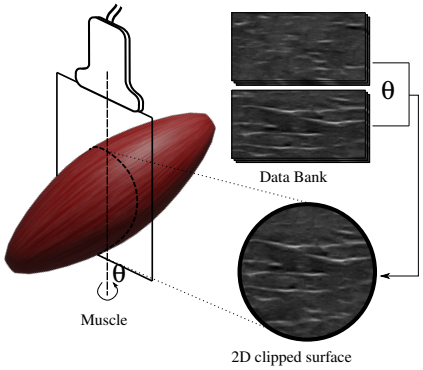

Figure 6: Creation of a muscle's US image by using texture from a data bank (with lateral and longitudinal textures) according to its orientation (measured by θ) to the probe.

Pre-computation. The first (pre-computed) step is to retrieve the orientation of the fiber. It is calculated

for all vertices thanks to the specific geometry of tendon-like tissue. Indeed, tendons present a curved cylindrical shape, in which the fibrous lines follow the direction of the curve. Thus, the direction is set by the smallest principal curvatures via quadratic fitting (Panozzo et al., 2010). This direction is then normalized and stored as a 3D vector.

Then, during the generation of the ultrasound view, the oriented blur used for thin tissues works in two phases (see Fig. 7).

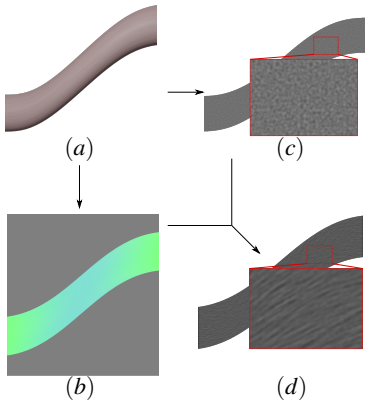

Figure 7: *Oriented blur* method: (a) a 3D tendon-like tissue is transformed into (d) a fibrous tissue on the 2D US view using (b) its RGB curvature map and (c) its noisy 2D image.

First GPU pass. The considered 3D tissue (Fig. 7a) is clipped in the ultrasound plane according to the probe position, and its surface is colored according to the orientation of the fibers (Fig. 7b). For our 3D scene, Fig. 4d displays the orientation of the fibers of the tendon. This created image will be readable by the GPU later on. For this result, the normalized three-dimensional curvature direction is mapped into the three-dimensional (RGB) color space. Hence, the gray color corresponds to the null vector. Since it accounts for the orientation of the probe, this step cannot be pre-calculated.

Second GPU pass. The created image (Fig. 7b) is used as an input to post-process the noisy image (Fig. 7c) to create the oriented blur (Fig. 7d): an inverse mapping on the input image gives the blur direction for each pixel of the noisy image. Then, a 1D convolution kernel to calculate the mean of 9 pixel values in the direction is used.

This technique fully uses the noise coming from the non homogeneous properties of the tissue (for a tissue with a plain original color, the oriented blur would not change the color of the pixel). Let's note that some US images are also being subject to a more classic radial blur. While this effect is more noticeable in abdominal ultrasound where the probe will scan for deep tissues, the distortion of the bottom part of the US image is still present in the reference image.

To achieve this, the image from Fig. 4c is post-processed to be rendered multiple times with radial offset. The center of rotation is given by the ultrasound probe, and the higher the angle, the less sharp the image is rendered. For our 3D scene, both the oriented and radial blur can be seen in Fig. 4e: the radial blur effect is more noticeable at the bottom of the picture, while our *oriented blur* effect is only present in the tendon.

Final US image w/o absorption. To end the rendering pass, the blurred picture (Fig. 4e) was mixed with the image obtained with the reflection and shadow effects (Fig. 4b) to create the final picture (Fig. 4f). See Fig. 5b for the same final image with absorption.

5 Haptic rendering

As previously said, two haptic devices were integrated in our framework. They simulate the manipulation of the needle and the probe to give the user the sense of touch thanks to forces applied to the devices. To get a smooth haptic feedback, the contact forces must be updated at around 1,000 Hz. As a result, the force feedback algorithm runs in its own thread for both the needle and the probe. Furthermore, their behaviors differ enough to handle them separately within the simulator (see Fig. 2): the probe interacts with the surface skin and supplies the plane for the ultrasound rendering, while the needle provides puncture forces and interacts with all tissues.

In this section, we will present the force feedback algorithms for both devices. The generated forces presented here will be used in the next section to create the tissue deformation in the ultrasound view.

Collision detection. The first step in haptic rendering is the detection of the collision between the haptic device and the objects in the 3D scene. We use the same collision thread for both the needle and the probe, as long as the needle does not pierce the first layer of an object. Usually, the collision is detected after it already occurred, by using volumes interpenetration or by checking if the haptic point is inside an object.

For example, Fig. 8 illustrates the collision detection with a needle having a velocity $\mathbf{v}$. A collision point is calculated afterward, using the minimal distance to surface (leading to point C), or the intersection of the needle shaft and the surface (leading to point B). However, it means that the real collision point is actually never registered, which could generate accuracy errors in its exact position if the needle is moving before registration. While this inaccuracy may be fine for the sole haptic thread, the visualization of the deformation that depends on this collision

point would suffer: an offset could appear between the needle and the deformed tissues.

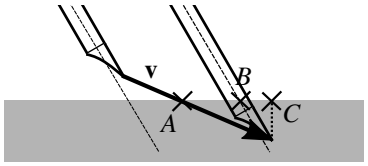

Figure 8: Collision point detection using a ray-casting following the velocity **v**. A is our detection point, B is the detection point along the shaft, C is the detection point with minimal distance to the surface of the virtual object.

To prevent this, we use a ray-casting method and a *Bounding Volume Hierarchy* on the surface triangles to detect precisely the collision point, even though this level of precision will mostly be used for the force feedback and accuracy of the needle. Below a critical distance between the device and the triangular surface of the virtual object, a collision point is created (and constantly updated) by taking into account the direction of the device's velocity (leading to point A). Then, barycentric coordinates in the detected triangle of the collision point are stored, along with the normal of the triangle. This information allows us to detect whether the device is above or touching the object during haptic rendering.

After that, the behaviors of the devices naturally differ when they are moving below the plane containing the detected triangle.

Probe haptic rendering. During the penetration of the surface plane by the haptic device, a classic *God-Object* (Zilles and Salisbury, 1995) is created for the probe. It is constrained to remain above the plane, to avoid unwanted display with the probe penetrating the tissues. From this point, the *God-Object* replaces the haptic interface in the rendering pass. While it only impacts the visual on the 3D scene, it serves for the overall immersion in the virtual world. Naturally, the *God-Object* is updated to follow the path of the probe, and can slide and rotate over the collided object.

Then, to get the haptic rendering of the probe, a simple stiffness force is calculated based on the elastic properties of the biological tissue, characterized by a stiffness K. This force $\mathbf{f_s}$ is normal to the probe and depends on the distance x between the haptic interface and the *God-Object*, with:

$$\mathbf{f_s}(x) = \begin{cases} 0, & x \leq 0 \\ Kx\,\mathbf{n}, & x > 0 \end{cases} \tag{3}$$

where $\mathbf{n}$ is the unit vector following the normal of the collided triangle, $K = 0.5$ N/mm for the skin (Ni et al., 2011). Moreover, as transmission gel is applied between the skin and the probe, the tangential part of the friction force is kept to 0 N. As a result, the probe can move freely on the object surface (and small friction force may be added on demand).

Needle haptic rendering. During insertion, the needle involves several force models and may go through multiple tissues. We followed Okamura which thoroughly studied this phenomena for liver tissue (Okamura et al., 2004). Let $\mathbf{f_s}$, $\mathbf{f_c}$, $\mathbf{f_f}$ be the forces due to stiffness, cutting and friction, respectively. Let x be the distance between the puncture point and the tip of the needle. The global force $\mathbf{f_g}$ along the needle shaft (with $\mathbf{u}$ its corresponding unit vector) is defined by:

$$\mathbf{f_g}(x) = \mathbf{f_s}(x) + \mathbf{f_c}(x) + \mathbf{f_f}(x). \tag{4}$$

Stiffness force. During the pre-puncture step, the stiffness force intensity $\|\mathbf{f_s}\|$ is steadily increasing until the puncture occurs (*i.e.* as long as $\|\mathbf{f_s}(x)\| < f_p$, with f_p the intensity of the necessary force to puncture the interface). At this point, a sharp resistance loss is detected involving $\|\mathbf{f_s}(x)\| = 0$ until a new interface is met. Following Okamura, we chose to approximate the pre-puncture stiffness force $\mathbf{f_s}$ with a second-order polynomial leading to:

$$\mathbf{f_s}(x) = \begin{cases} 0, & x \leq 0 \\ (K_1 x + K_2\, x^2)\,\mathbf{u}, & x > 0 \end{cases} \tag{5}$$

where K_1, K_2 are parameters chosen according to tissues. Even if this force modeling is vastly used, specific parameter data per tissues are rarely given. Indeed, even in (Okamura et al., 2004), those parameters differed for the same tissue between tests. This problem has been tackled in a survey (van Gerwen et al., 2012): without massive experimental data, the only option is to trust the haptic sense from multiple experts to tune the parameters K_1, K_2 according to their own feedback sensation during their experiment on the simulator.

Cutting force. After puncture, the cutting force is involved to slice through the tissue. It combines the fracture force needed to create the path for the needle, and the stiffness force of the tip of the needle on the tissue. It is usually isolated by puncturing the exact same path twice and subtracting the two global forces. The cutting force is approximated by a constant, if the needle velocity is not zero, with:

$$\mathbf{f_c}(x) = f_c\,\mathbf{u}. \tag{6}$$

Friction force. A wide number of friction models exists (Yang et al., 2018). Following (Okamura et al., 2004), a modified Karnopp model is used:

$$\mathbf{f_f}(\dot{x}) = \begin{cases} (C_n\, sgn(\dot{x}) + b_n\, \dot{x})\,\mathbf{u}, & \dot{x} \leq -\Delta v/2 \\ (max(D_n, F_a))\,\mathbf{u}, & -\Delta v/2 < \dot{x} \leq 0 \\ (min(D_p, F_a))\,\mathbf{u}, & 0 < \dot{x} < \Delta v/2 \\ (C_p\, sgn(\dot{x}) + b_p\, \dot{x})\,\mathbf{u}, & \dot{x} \geq \Delta v/2 \end{cases} \tag{7}$$

where C_n, C_p are negative and positive values of dynamic friction; b_n, b_p are negative and positive damping coefficients (depending on the needle diameter and the depth of the needle in the tissue); D_n, D_p are negative and positive values of static friction; $\dot{x}$ is the relative velocity between the needle and the tissue; $\Delta v/2$ is the threshold below which the velocity is considered to be 0; F_a is the sum of non frictional forces applied to the system.

Tunnel effect. In addition to the usual forces in haptic needle insertion, we constrain the needle on a path during the puncture (see Fig. 9). It serves the purpose of improving the force feedback realism with the addition of a force perpendicular to the needle shaft.

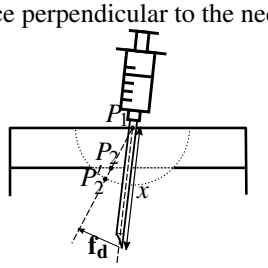

Figure 9: Constraint points and *tunnel effect*.

The first constraint (P_1) is the skin collision point. It is acting as a ball joint combined with a sliding part. The needle can only slide at the collision point and no tangential movement is allowed. While right under the skin surface, the user is free to rotate the needle to adapt his direction path. But as soon as the user is exceeding a given depth (P_2') or when another tissue is punctured (P_2), a new constraint is created. The two combined constraints create a linear path that the needle will be constrained to follow. Any deviation creates a force feedback $\mathbf{f_d}$ simulating the elastic behavior of the tissue with the same stiffness K. This force is the only one perpendicular to the needle shaft direction. It is defined by:

$$\mathbf{f_d} = -\frac{K}{l}\, x \left(\mathbf{x} - (\mathbf{x} \cdot \mathbf{P_1P_2}) \, \frac{\mathbf{P_1P_2}}{||\mathbf{P_1P_2}||^2} \right), \quad (8)$$

with $\mathbf{x}$ the vector of length x between P_1 and the tip of the needle, l the full length of the needle. The first constraint P_1 is of significant importance, as it will dictate the overall behavior of the needle (hence the need for precision in the collision thread). This constraint is linked to the collided triangle and must be updated during any displacement or deformation of the considered triangle.

Furthermore, when multiple layers of tissue are punctured, the force is the sum of the combined efforts of the tissues. For each tissue, the friction force is weighted by the needle length traversing it. Note that stiffness and cutting forces only appear at the layer of the needle tip (and that the stiffness force will disappear as soon as no layer interface is intersected).

6 Tissue deformation shader

The last step consists in taking into account the velocity and the force feedback of the two haptic devices in the rendering process. Indeed, the challenge is to visualize the tissue deformation in the ultrasound view during gesture. We detail here our original solution based on displacement fields.

General approach. The force feedback and velocity of the needle/probe can be linked to the displacement of the surrounding tissues by simple equations. This approach is based on observation and function fitting (Gao et al., 2013; Crouch et al., 2005). Then, the 3D displacement function is directly mapped to the 2D image. It avoids the 3D physical simulation of soft tissues and interactions with medical instruments, that is barely compatible with real-time.

Rendering pipeline. In our rendering, there are two phases to obtain the deformations in the US view: (i) the 2D ultrasound is rendered into an image (see Section 4); (ii) this image is displayed on the screen. However, between these two steps, post-processing effects may be applied on the GPU.

Let's consider a pixel P of the 2D image with basic coordinates (u,v). With no additional effect, the screen exactly displays the image of the rendered scene. Now if we want to render the pixel P with an offset given by a displacement function d, we only have to apply this displacement at P. Thus, we obtain its new position $d(P) = P'$ of coordinates (u',v'). A heatmap is often used to highlight the displacement intensity (Fig. 11b or c, with a blue-red scale).

The first step consists in defining the 3D displacement function (noted $d(x,y,z)$ in the world space) corresponding to the wanted effect (needle insertion or probe contact); then, the 2D section corresponding to the ultrasound plane is retrieved and we apply the corresponding displacement (noted $d(u,v)$ in the image space) on each pixel. Note that the displacement function is first computed in 3D, allowing us to see the influence of the needle on the tissues, even if the needle itself is not visible in the 2D plane. At the end, the conversion (much like for the orientation blur process) transforms the sectioned deformation function into a texture readable by the GPU (see Fig. 10).

To improve realism, we consider several elastic behaviors of soft tissues. To illustrate our process, Fig. 11 presents an example for one section of a simple 2-layered 3D scene, where a texture grid was added to better follow the displacement. The Young modulus E of each tissue is given by its gray value. Each pixel of the image (Fig. 11a) is moved following the value of the displacement function, which depends of the Young modulus. Moreover, a mean value with neighbor pixels is performed to ensure displace-

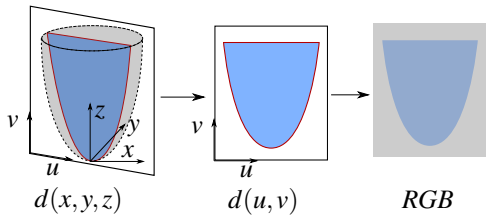

Figure 10: (i) The displacement function $d(x,y,z)$ is defined in the 3D world space. (ii) It is transformed in $d(u,v)$ in the US image space. (iii) The corresponding texture is stored.

ment continuity at the interface between two highly different values of E. At the end, the difference could be appreciated when using a single (Fig. 11b) or several values (Fig. 11c) of E. Under normal conditions, the texture grid is replaced by the US render and the Young modulus information is given by a 2D slice image with a gray shading for each tissue (calculated and stored at the same time as the diffuse color - Fig. 4a).

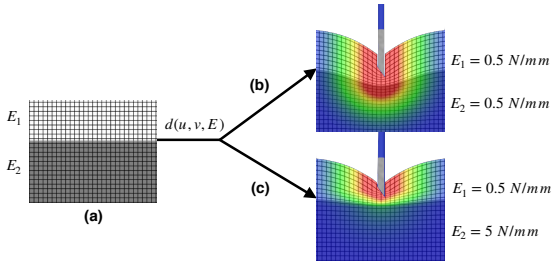

Figure 11: Displacement function $d(u,v,E)$ applied on image (a) resulting to image (b) or (c) according to E value.

At this point, the issue is to find fitting and configurable displacement functions $d(x,y,z,E)$ in the world space to simulate the deformation due to the needle insertion and the probe according to the elastic behavior of the tissue.

Displacement due to the needle. The deformation due to the needle can be decomposed into two parts: (i) the skin deformation before and during puncture; (ii) the inner tissues deformation after puncture.

Skin deformation. Intensive work on the deformation of the skin has been made by Gao *et al.* (Gao et al., 2013). Even though the experiment took place with an artificial tissue and at fixed velocity of 2.5 mm/s, it shows a relationship between the needle displacement and the deformed volume of the skin. We used those results to simulate the deformation of the skin and subcutaneous tissues during elastic deformation due to the stiffness force.

Inner tissues deformation. The deformation of subcutaneous tissues is only visible in the 2D ultrasound view. During needle displacement, friction forces between the needle and the biological tissue cause a deformation of the latter that only affects the surrounding area, with no (or negligible) deformation outside of it. This area has been studied in (Crouch et al., 2005). Their model allows us to use the deformation function of the tissue close to the needle during displacement, and to display it in real-time during the US image rendering step.

Displacement functions. To further match the observation and forces calculated by haptic rendering, the displacement function for the needle insertion is split into two: before/after puncture of its layer. And, the displacement functions are defined to visually fit the model of (Gao et al., 2013) and (Crouch et al., 2005).

Let $\tilde{r}$ be the cylindrical coordinate r, when $z < z_{max}$ (point A) and $\tilde{r}$ be the spherical coordinate r when $z > z_{max}$ (point B) (see Fig. 12). Before puncture, as the needle pushes the surface, the displacement of the tissue at the tip of the needle is exactly equal to the displacement of this same tip. Indeed, the pre-puncture elastic force is dominant until the puncture occurs. This displacement also affects the tissues under the puncture point. It is defined by:

$$d(\tilde{r},z,E) = \begin{cases} z_{max}\, g\left(2 - \frac{\tilde{r}}{R_{max}}\right), & z < z_{max} \\ \frac{\|\mathbf{f_s}\|}{E}\, g\left(\frac{\tilde{r}}{R_{max}}\right), & z > z_{max} \\ 0, & \tilde{r} > R_{max} \end{cases} \quad (9)$$

where $g(t) = 1 - (3t^2 - 2t^3)$, $\mathbf{f_s}$ is the stiffness force, E is the Young modulus of the tissue at the point $(\tilde{r},z)$. R_{max} is the influence radius of the needle from Crouch's model (with $R_{max} = 2cm$).

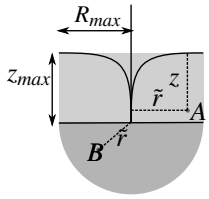

Figure 12: Two zones of effect for the displacement function: along (light gray) / beneath (dark gray) the needle tip.

After puncture, the friction and cutting forces affect the tissues along the shaft and the ones below the needle. Locally, the friction force is dominant along the shaft, while the cutting force is dominant under the tip. It means that we can also split our displacement function in two. It is defined by:

$$d(\tilde{r},z,E) = \begin{cases} \frac{\|\mathbf{f_f}\|}{z_{max}\,E}\, g\left(2 - \frac{\tilde{r}}{R_{max}}\right), & z < z_{max} \\ \frac{\|\mathbf{f_c}\|}{E} g\left(\frac{\tilde{r}}{R_{max}}\right), & z > z_{max} \\ 0, & \tilde{r} > R_{max} \end{cases} \quad (10)$$

where $\mathbf{f_f}$ and $\mathbf{f_c}$ are the friction and cutting force given by the haptic device simulating the needle. Let's remark that $\mathbf{f_f}$ is divided by z_{max} as the friction force is spread along the needle.

Displacement due to the probe. The probe deforms the tissue on a global scale, proportionally to the pressure exerted on the skin. An interesting study has been made by (Flack et al., 2016), which records the probe position during acquisition to deduce the exerted pressure, and apply reverse displacement onto the US images. However, the studied abdominal image exhibit much larger deformations than ours. Due to US images generation process and pressure of the probe, the soft tissue are always subject to displacement during acquisition. At the difference of abdominal probe, the ones used for shoulder joint are flat. Thus, an uniform force could be applied at the surface of the skin, and the displacement function results in:

$$d(z) = \frac{\|\mathbf{f_s}\|}{E(1+z)}, \tag{11}$$

where $\mathbf{f_s}$ is the stiffness force given by the haptic device simulating the probe. Let's note that this displacement function is added to the one of the needle.

7 Results

Our complete simulator. Fig. 13 presents a picture of our simulator. For this first prototype, we used an Intel® Core™ i7-6800K CPU, an NVIDIA® GeForce® 1070GTX and 31.3 GB of memory. The haptic devices were respectively a Touch™ 3D stylus and a Geomagic® Touch™. Fig. 13 also shows the two main views proposed by the graphical rendering: (i) a pedagogical 3D views (showing interactions between organs and needle) which permit to infer internal location of the tissues and needle, with their displacements; (ii) our 2D ultrasound view, including the tissue deformation, similar to the one provided by the probe used by rheumatologists during the gesture.

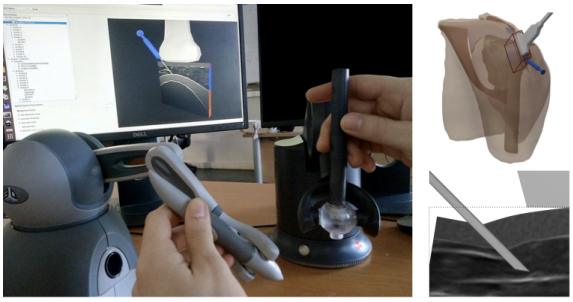

Figure 13: Our simulator which couples a graphical rendering with two haptic devices simulating probe and needle. (up) 3D models (shoulder-probe-needle); (down) zoom on tissue deformation with ultrasound view.

US rendering. Fig. 14 presents the reference image used to create our 3D scene and the US image generated by our method for the clipping zone of the 3D scene defined according to the probe position.

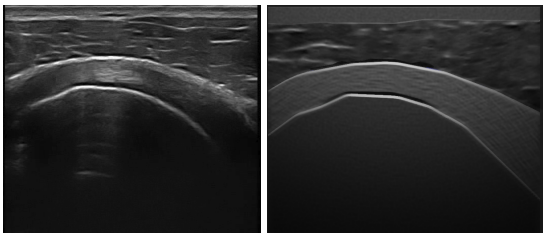

Figure 14: (left) US reference image. (right) The ultrasound image generated by our process (without deformation).

Fig. 15 shows some results obtained for the displacement of the soft tissues, due to the needle or the probe, considering a single or two values of E for the tissues ($E = 0.5$ and $5N/mm$ for top and bottom layers). Note that on Fig. 15b, the tissues on the sides are out of the scope of the probe, so they follow the global uniform force for simplicity reasons but without any influence on the final result, as seen on Fig. 16 which presents our final US rendering. On this figure, we can see the tissue deformation due to the forces involved by haptic devices (probe or needle): they are used to alter the texture, allowing a realistic real-time display of the tissue deformation on the US image.

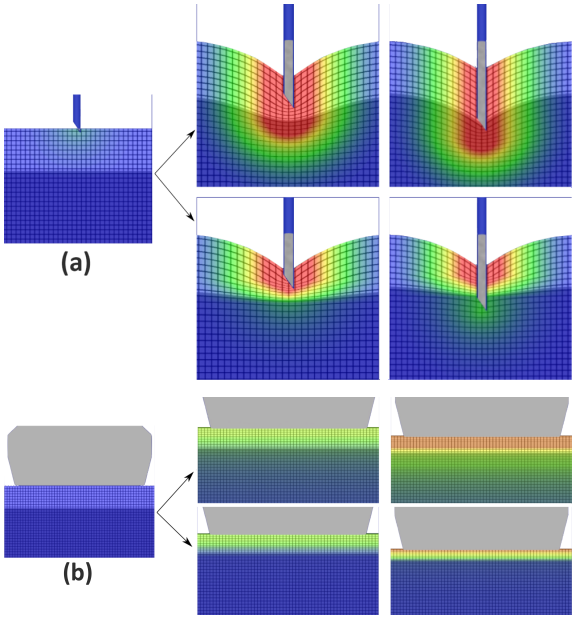

Figure 15: Deformation due to (a) the needle and (b) the probe considering a single (top row) or two values of E (bottom row) for tissues.

Performance. Several tests were performed on a simple scene, involving a sphere with an increasing

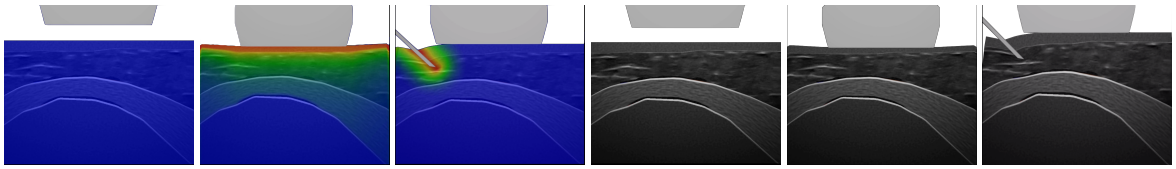

Figure 16: Final US images showing the probe or the needle tissue deformation (w/ or w/o the superposed heatmap).

amount of triangles. The sphere acted as a fibrous object under deformation. The recorded times (Fig. 17) are the mean of the first 120 simulation frames. The results are presented for all render steps (with probe and needle) as described in this paper (from the creation of the US image to the deformation).

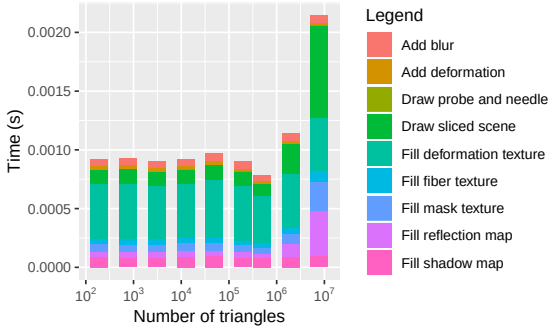

Figure 17: Cumulated time (in seconds) of all the render steps *versus* the numbers of triangles (log scale).

Even for $7,864,320$ triangles, our rending runs in about 0.002 s with all the effects, which is more than enough for real-time simulation ($\approx$0.06 s). To compare those results with other existing approaches on US image generation with mesh deformation, we ran the tests again, but this time we filled the GPU buffer at each frame (Fig. 18), which took 50% to 99% of time relative to the creation of a frame (Fig. 19).

Even if this last step is not necessary in our method (which is one of its strong points), it would be mandatory in case of an update of the vertex positions, as in classical methods. This comparison is the closest we were able to imagine while avoiding a tedious implementation of a physically-based soft tissue deformation system.

The haptic thread itself always runs at around 500 Hz. While lower than the usual frequency of 1,000 Hz, none of the 2 haptic devices has shown parasitic vibrations.

8 Discussion

The pipeline presented here allows us to create an US image from any biological tissue model and from any probe location and orientation. We avoid the construction of a specific database that might be very dependent on a considered joint or on the location of inflammatory tissues. The rendering goes through several steps, including shadow, reflection, noise, attenuation and it includes the rendering of fiber orientation, which to our knowledge has never been presented before in a real-time simulation. Instead of modeling the fibrous tissue, we used a texture-based oriented blur. The ultrasound rendering pass is also completely embedded into the classic 3D scene render pass. Thus, both 3D and US 2D views can be rendered, at the same time, without any loss of performance. It allows for a slightly augmented immersion sense for the user, and should lead to an improvement of the pedagogical path. In related work, we have seen the benefits of the generative approach to create the ultrasound image, thanks to its flexibility, even if they still lack some realism when done in real-time environment. To overcome this, we managed to add the fibrous structure to better identify the biological tissue.

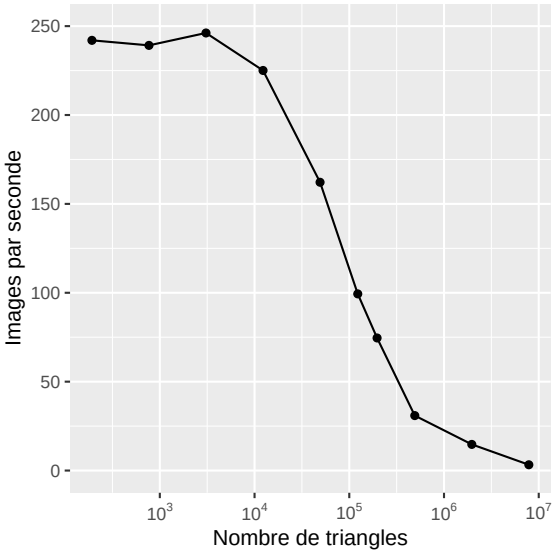

Figure 18: Loss in FPS in the classical approach with buffer filling *vs* the number of triangles (in log scale).

Future work will focus on enhancing the visual of the inner structure of non-fibrous tissue, such as the subcutaneous fat, which still lacks details. Voronoi noise is a possible solution. Moreover, when we compare the final image with the reference (see Fig. 14),

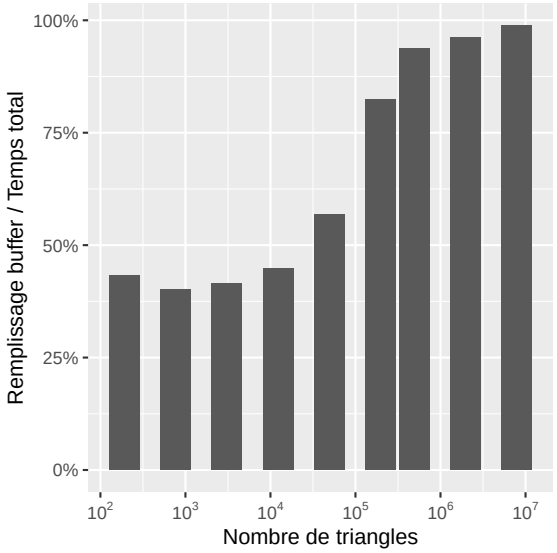

Figure 19: Percentage of time allocated to the refill of the buffer relative to the time of creation of a frame.

we can observe a difference in lighting. Strong echoes in some probe orientations produce repetitive light pattern that are not yet generated in our model.

Concerning the evaluation and comparison of our images with previous work, it is proved to be difficult due to the different choices of body region and the subjectiveness on the quality. Therefore, the details, ultrasound effects and overall evaluation of our images is in course with subject-matter experts, but is beyond the scope of this paper.

About tissue deformation, we have seen in related work a few real-time needle insertion simulation with haptic, but always on reduced models. The use of displacement function directly on the image allows us to work with complex models without increasing computational time. The complexity of the model will only slightly increase the time to render the mesh. However, the displacement functions accuracy depends of a deformation model, which means that they can't reproduce any deformation or displacement that does not fit their model. For example, the current model is not appropriate for very low of fast velocity, and lack realism in the relaxation phase. This trade-off is believed to be the price to pay to cope with performances required in real-time environment.

9 Conclusion and perspective

In this paper, we presented a new way to create an ultrasound rendering suitable for a needle insertion training simulator. Our strategy enables to show, in the ultrasound view, the deformation induced by the use of two haptic devices which correspond to the probe and the needle usually used by rheumatologists.

Our proposition brings some breakthroughs. Firstly, it avoids the use of a 3D volume texture database. This permits to easily consider several medical cases, that can be easly tuned according to the chosen scenario: several joints (knee, shoulder), various patient morphology, various pathologies with inflamed tissues, etc. Secondly, it permits to display the tissue fibers and their orientation in the ultrasound view. This point visually improves the existing solutions in ultrasound rendering. Thirdly, our approach enables to show the tissue deformations due to the needle insertion. To that end, our solution deals with the use of textures and displacement models to take advantage of the GPU for a complete real-time solution.

For the haptic rendering, a continuous collision detection was used to accurately detect the real collision point between device and tissues. Then, haptic puncture forces were calculated using the constrained points allowing a realistic deformation inside the US view, leading to improve the learner immersion sense.

Next step will aim to further improve the visual rendering of the US image by adding others artifacts, and add more complex and precise displacement force, based on physically-based simulations.

REFERENCES

Abolhassani, N., Patel, R., and Moallem, M. (2007). Needle insertion into soft tissue: A survey. *Medical engineering & physics*, 29(4):413–431.

Bamber, J. and Dickinson, R. (1980). Ultrasonic B-scanning: a computer simulation. *Physics in Medicine & Biology*, 25(3):463.

Burger, B., Bettinghausen, S., Radle, M., and Hesser, J. (2013). Real-time gpu-based ultrasound simulation using deformable mesh models. *IEEE transactions on medical imaging*, 32(3):609–618.

Crouch, J. R., Schneider, C. M., Wainer, J., and Okamura, A. M. (2005). A velocity-dependent model for needle insertion in soft tissue. In *International Conference on Medical Image Computing and Computer-Assisted Intervention*, pages 624–632. Springer.

DiMaio, S. P. and Salcudean, S. E. (2003). Needle insertion modeling and simulation. *IEEE Transactions on robotics and automation*, 19(5):864–875.

Duriez, C., Guébert, C., Marchal, M., Cotin, S., and Grisoni, L. (2009). Interactive simulation of flexible needle insertions based on constraint models. In *International Conference on Medical Image Computing and Computer-Assisted Intervention*, pages 291–299. Springer.

Flack, B., Makhinya, M., and Goksel, O. (2016). Model-based compensation of tissue deformation during data acquisition for interpolative ultrasound simulation. In *Biomedical Imaging (ISBI), 2016 IEEE 13th International Symposium on*, pages 502–505. IEEE.

Gao, D., Lei, Y., and Yao, B. (2013). Analysis of dynamic tissue deformation during needle insertion into soft tissue. *IFAC Proceedings Volumes*, 46(5):684–691.

Goksel, O. and Salcudean, S. E. (2009). B-mode ultrasound image simulation in deformable 3-D medium. *IEEE transactions on medical imaging*, 28(11):1657–1669.

Harrison, P. (2001). A non-hierarchical procedure for re-synthesis of complex textures. *WSCG '2001: Conference proceedings: University of West Bohemia, Plzen, Czech Republic*, pages 190–197.

Heer, I., Middendorf, K., Müller-Egloff, S., Dugas, M., and Strauss, A. (2004). Ultrasound training: the virtual patient. *Ultrasound in Obstetrics and Gynecology*, 24(4):440–444.

Jensen, J. A. (1991). A model for the propagation and scattering of ultrasound in tissue. *The Journal of the Acoustical Society of America*, 89(1):182–190.

Law, Y. C., Ullrich, S., Knott, T., Kuhlen, T., and Weg, S. (2011). Ultrasound image simulation with gpu-based ray tracing. *Virtuelle und Erweiterte Realität*, 8:183–194.

Magee, D. and Kessel, D. (2005). A computer based simulator for ultrasound guided needle insertion procedures. *IEE International Conference on Visual Information Engineering (VIE 2005)*, pages 301–308.

Magee, D., Zhu, Y., Ratnalingam, R., Gardner, P., and Kessel, D. (2007). An augmented reality simulator for ultrasound guided needle placement training. *Medical & biological engineering & computing*, 45(10):957–967.

Marion, A. and Vray, D. (2009). Toward a real-time simulation of ultrasound image sequences based on a 3-d set of moving scatterers. *IEEE transactions on ultrasonics, ferroelectrics, and frequency control*, 56(10):2167–2179.

Mattausch, O. and Goksel, O. (2016). Monte-carlo ray-tracing for realistic interactive ultrasound simulation. In *Proceedings of the Eurographics Workshop on Visual Computing for Biology and Medicine*, pages 173–181. Eurographics Association.

McReynolds, T. and Blythe, D. (2005). *Advanced graphics programming using OpenGL*. Elsevier.

Ni, D., Chan, W. Y., Qin, J., Chui, Y.-P., Qu, I., Ho, S. S., and Heng, P.-A. (2011). A virtual reality simulator for ultrasound-guided biopsy training. *IEEE Computer Graphics and Applications*, 31(2):36–48.

Okamura, A. M., Simone, C., and O'leary, M. D. (2004). Force modeling for needle insertion into soft tissue. *IEEE transactions on biomedical engineering*, 51(10):1707–1716.

Panozzo, D., Puppo, E., and Rocca, L. (2010). Efficient multi-scale curvature and crease estimation. *Proceedings of Computer Graphics, Computer Vision and Mathematics (Brno, Czech Rapubic*, 1(6).

Takabi, B. and Tai, B. L. (2017). A review of cutting mechanics and modeling techniques for biological materials. *Medical engineering & physics*, 45:1–14.

van Gerwen, D. J., Dankelman, J., and van den Dobbelsteen, J. J. (2012). Needle–tissue interaction forces–a survey of experimental data. *Medical engineering & physics*, 34(6):665–680.

Vidal, F. P., John, N. W., Healey, A. E., and Gould, D. A. (2008). Simulation of ultrasound guided needle puncture using patient specific data with 3D textures and volume haptics. *Computer Animation and Virtual Worlds*, 19(2):111–127.

Yang, C., Xie, Y., Liu, S., and Sun, D. (2018). Force modeling, identification, and feedback control of robot-assisted needle insertion: a survey of the literature. *Sensors*, 18(2):561.

Zilles, C. B. and Salisbury, J. K. (1995). A constraint-based god-object method for haptic display. In *Intelligent Robots and Systems 95.'Human Robot Interaction and Cooperative Robots', Proceedings. 1995 IEEE/RSJ International Conference on*, volume 3, pages 146–151. IEEE.